

Progress Report – Year2

Project Title:

Experimental Study of hypersonic wing/fin root heating at Mach 8

Key Researcher:

Professor Michael K. Smart
Chair of Hypersonic Propulsion
The University of Queensland
Ph: +61 7 3365 3783
m.smart@uq.edu.au

School of Mechanical and Mining Engineering
The University of Queensland
St Lucia, Brisbane. 4072
Australia

Report Documentation Page			Form Approved OMB No. 0704-0188		
Public reporting burden for the collection of information is estimated to average 1 hour per response, including the time for reviewing instructions, searching existing data sources, gathering and maintaining the data needed, and completing and reviewing the collection of information. Send comments regarding this burden estimate or any other aspect of this collection of information, including suggestions for reducing this burden, to Washington Headquarters Services, Directorate for Information Operations and Reports, 1215 Jefferson Davis Highway, Suite 1204, Arlington VA 22202-4302. Respondents should be aware that notwithstanding any other provision of law, no person shall be subject to a penalty for failing to comply with a collection of information if it does not display a currently valid OMB control number.					
1. REPORT DATE 27 DEC 2012		2. REPORT TYPE Final		3. DATES COVERED 29-06-2010 to 28-06-2012	
4. TITLE AND SUBTITLE Experimental Study of hypersonic wing/fin root heating at Mach 8			5a. CONTRACT NUMBER FA23861014124		
			5b. GRANT NUMBER		
			5c. PROGRAM ELEMENT NUMBER		
6. AUTHOR(S) Michael Smart			5d. PROJECT NUMBER		
			5e. TASK NUMBER		
			5f. WORK UNIT NUMBER		
7. PERFORMING ORGANIZATION NAME(S) AND ADDRESS(ES) The University of Queensland,Centre for Hypersonics,QLD, Australia 4072,Australia,NA,NA			8. PERFORMING ORGANIZATION REPORT NUMBER N/A		
9. SPONSORING/MONITORING AGENCY NAME(S) AND ADDRESS(ES) AOARD, UNIT 45002, APO, AP, 96338-5002			10. SPONSOR/MONITOR'S ACRONYM(S) AOARD		
			11. SPONSOR/MONITOR'S REPORT NUMBER(S) AOARD-104124		
12. DISTRIBUTION/AVAILABILITY STATEMENT Approved for public release; distribution unlimited					
13. SUPPLEMENTARY NOTES					
14. ABSTRACT A series of tests were conducted at both ?low? and ?high? pressure conditions, representing atmospheric conditions at Mach 8 and a ?high heating? case respectively. Results exhibited good correlation in peak heating showing higher heating loads for both increases in pressure and decreases in sweep angle. While conclusions about flow topology remain to be made, an unexpected observation is that the shock impingement, or peak heating, occurred farther from the wing root when moving from a low to high pressure condition. Additionally the effect of the conditions on peak heating on the wing appeared to decrease with increasing sweep angle with the relative peak heating for a high pressure shot at 700%, 200% and 60% for 45?, 55? and 65? of sweep respectively.					
15. SUBJECT TERMS Hypersonics, Hypersonic Test Facilities , Shock Tunnels, wing-kinematics					
16. SECURITY CLASSIFICATION OF:			17. LIMITATION OF ABSTRACT Same as Report (SAR)	18. NUMBER OF PAGES 24	19a. NAME OF RESPONSIBLE PERSON
a. REPORT unclassified	b. ABSTRACT unclassified	c. THIS PAGE unclassified			

Abstract

The junction between wings or fins and the body of a high speed flight vehicle creates a complex 3-D shock wave/boundary layer interaction. In hypersonic flight this interaction can lead to localized high heating rates. While the general topology of this flow has been established, confidence in the heating rates predicted by CFD is not high. This study involves an extremely dense set of heat transfer measurements on a model consisting of a flat plate and a cylinder with an adjustable sweep angle. The tests were conducted in the T4 shock tunnel at conditions simulating Mach 8 flight at 30km altitude (~100k ft), which is the nominal condition for many flights in the HIFiRE Program. This dataset is intended to aid the development of design rules for wings, fins and struts on hypersonic vehicles and to be used for comparison to advanced CFD codes.

This is a progress report for Year 2 of the AOARD funded project “Experimental Study of hypersonic wing/fin root heating at Mach 8”.

A series of tests were conducted at both “low” and “high” pressure conditions, representing atmospheric conditions at Mach 8 and a “high heating” case respectively. Results exhibited good correlation in peak heating, showing higher heating loads for both increases in pressure and decreases in sweep angle. While conclusions about flow topology remain to be made, an unexpected observation is that the shock impingement, or peak heating, occurred farther from the wing root when moving from a low to high pressure condition. Additionally, the effect of the conditions on peak heating on the wing appeared to decrease with increasing sweep angle, with the relative peak heating for a high pressure shot at 700%, 200% and 60% for 45°, 55° and 65° of sweep respectively.

The next report will document a comparison between the results and analytical/computational models, and will attempt to infer the relative merit of both at these conditions based on the experimental campaign.

Contents

Progress Report – Year2	1
Experimental Study of hypersonic wing/fin root heating at Mach 8	1
Abstract.....	2
Project Status: September 2012.....	Error! Bookmark not defined.
Project Plan: 2011-2012.....	Error! Bookmark not defined.
Pay-off.....	Error! Bookmark not defined.
1. Model Design and Manufacture	4
1.1 Heat flux and thermocouple gauge recesses.....	4
1.2 Final design	5
2. Heat flux gauge design and construction	8
2.1 Preliminary design considerations and theory	8
2.2 Thin film Gauge construction.....	9
2.3 Thermocouple construction	11
3. Analytical heat flux calculations	12
4. Experimental Campaign	15
4.1 Tunnel Conditions	15
4.2 Results	17
4.2.1 Results at 45° of sweep.....	17
4.2.2 Results at 55° of sweep.....	19
4.2.3 Results at 65° of sweep.....	20
5. Summary	22
Bibliography	24

1. Model Design and Manufacture

The design of the wing root experiment began with an assessment of design considerations for the experiment and the parameters of the T4 shock tunnel facilities. A CAD image of the model is shown in Figure 1-1.

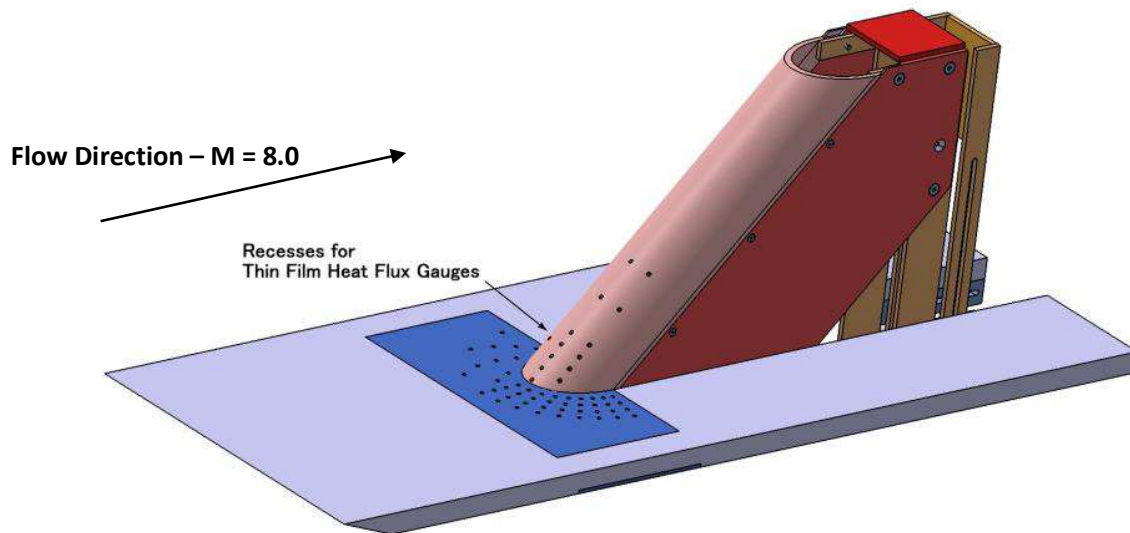


Figure 1-1: CAD view of wind tunnel model

The cylinder representing the wing or fin of a hypersonic vehicle was designed to allow for continuously varying sweep angles from 45° to 70° . The flat plate and leading edge, which represent the body of the hypersonic vehicle, were required to have a length sufficient to allow for the development of a turbulent incoming boundary layer, with consideration for the space limitations of the test section in the T4 shock tunnel facilities. The leading edge precedes the wing-root intersection by 200mm, and the plate is 150 mm wide. The length of the wing is 240mm, although the effective length will vary slightly depending on angle, as a certain fraction of the wing will be inside the body for lower sweep angles.

1.1 Heat flux and thermocouple gauge recesses

Measurement of heat flux during the experimental campaign will be conducted with the use of thin film gauges, using a 2mm cylindrical quartz substrate. These sensors will be mounted on the cylinder and flat plate, at expected points of interest near the wing root junction (see Figure 1-1). As the test facility is limited by the number of possible data channels, the experiment was limited to the implementation of 73 heat flux gauges on the initial design of the model. A further requirement was that the sensors do not appreciably interfere with the flow, and to this end great care was taken to mount the gauges flush with the surface of the wedge and flat plate. Further detail on the design of thin film and thermocouple gauges can be found in Section **Error! Reference source not found.** During implementation of the sensors it was decided to reduce the number of thin film gauges on the flat plate to 31. The resulting final configuration used in the campaign is shown in Figure 1-2 and Figure 1-3.

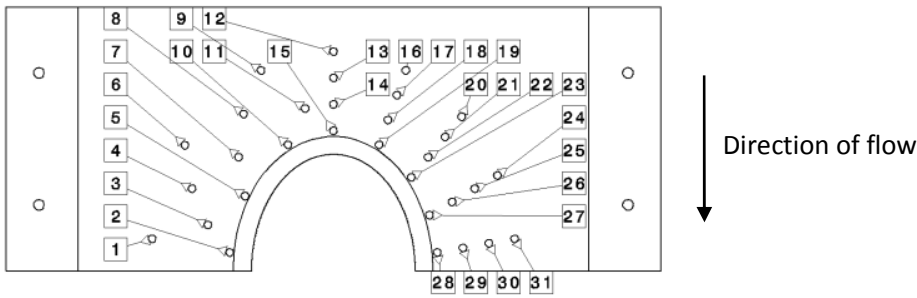


Figure 1-2: Flat plate recess numbering (all recesses are used for thin film gauges)

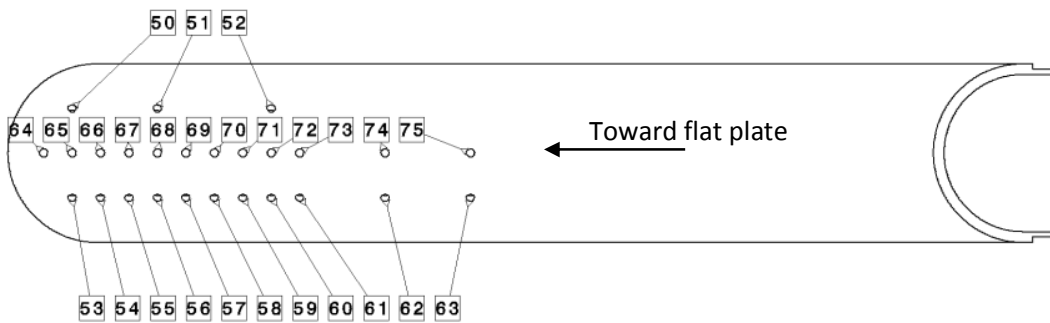


Figure 1-3: Wing recess numbering (recesses 50-63 used for thin film gauges, and recesses 68-73 used for thermocouples; the remaining recesses were sealed)

1.2 Final design

The final design of the wing root experiment is further illustrated in Figure 1-4, showing key dimensions. Note that the sweep angle θ is measured relative the direction normal to the freestream. Also, the model is inverted to allow for more stable and efficient mounting to the T4 test section.

The distribution of recesses for insertion of the thin film gauges can also be readily seen in Figure 1-4, indicated by the small points near the base of the wedge/flat plate intersection. Note that the gauge recesses are asymmetrically distributed; this is the case on both the blunt wedge (the wing) and the flat plate (the vehicle body) to take advantage of flow symmetry, allowing for the gauge responses to be superimposed onto both sides. This will allow us to map the resulting heat fluxes at a higher spatial resolution than would otherwise be possible due to the size and minimum distance between each of the 2mm gauges.

A photograph of the fully manufactured cylinder and flat plate components of the experimental model are shown in Figure 1-5.

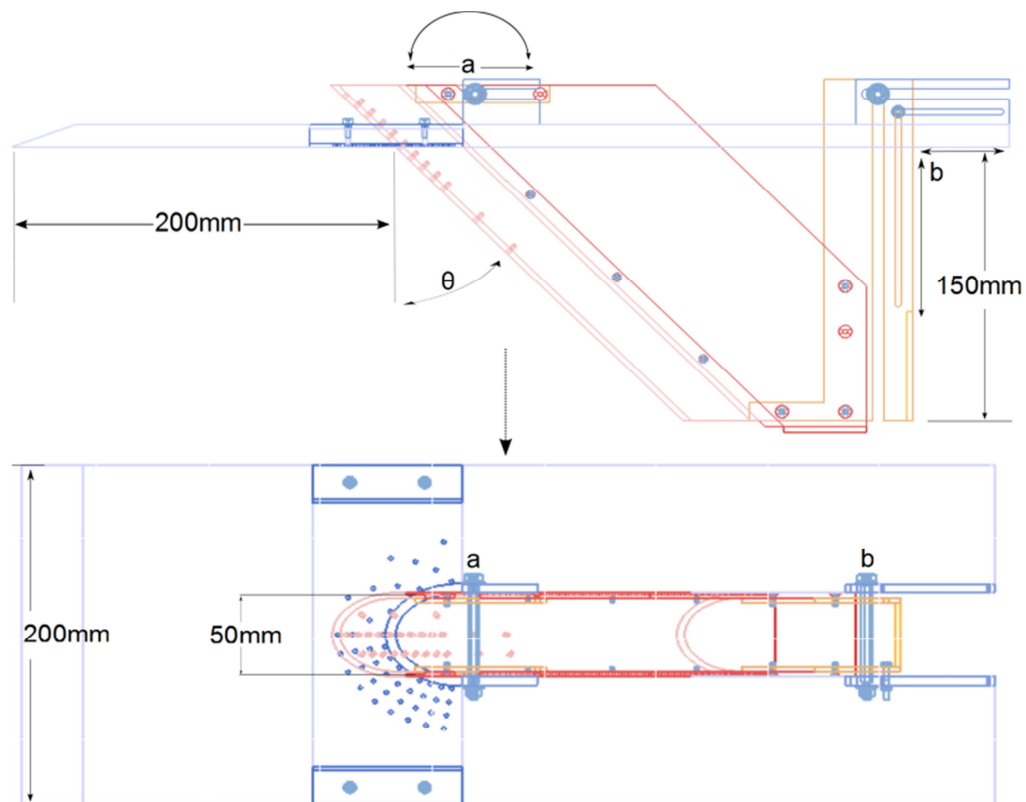


Figure 1-4: Top and side views of the wing root experiment design, showing the sliding pivot junctions (a and b) that allow for the wing sweep angle (θ) to vary continuously between sweep angles of 45° and 70°

Figure 1-5 shows the final model after all thin film gauges and thermocouples have been inserted, and the model has been placed in the tunnel. Note that the photo has been inverted, as the actual model was placed in the tunnel with the wing protruding downward. All images are shown with the wing extending upward for consistency with CFD models and other images. No reference to starboard and port directions will be made, as these would now be arbitrary and given that the experiment is symmetric it therefore not benefit from such a distinction.

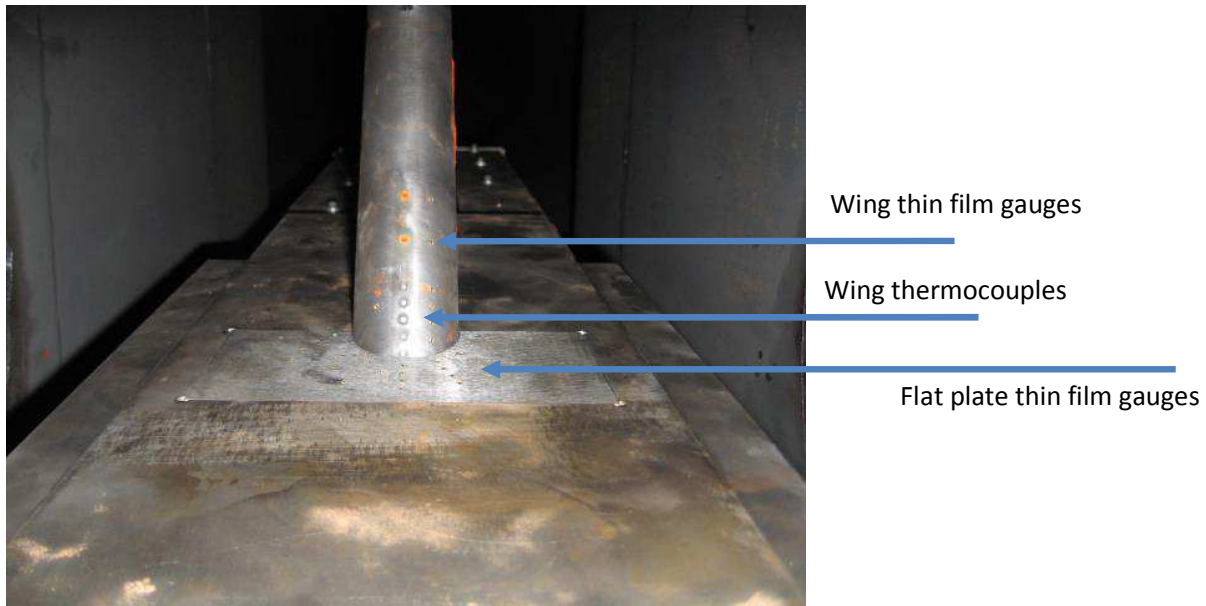


Figure 1-5: View of the model after insertion into the tunnel, and prior to the first shot (vertically inverted)

A significant portion of the experimental preparation involved the design of shielding components, which protected the internal components of the instrumentation while allowing the flow to pass over the shielding as freely as possible, so as to ensure that any perturbations caused by it do not interfere with the measurements. Experimental results did not suggest that any interference took place during the tests.

The final model, as mounted prior to the first shot, is shown in Figure 1-6.

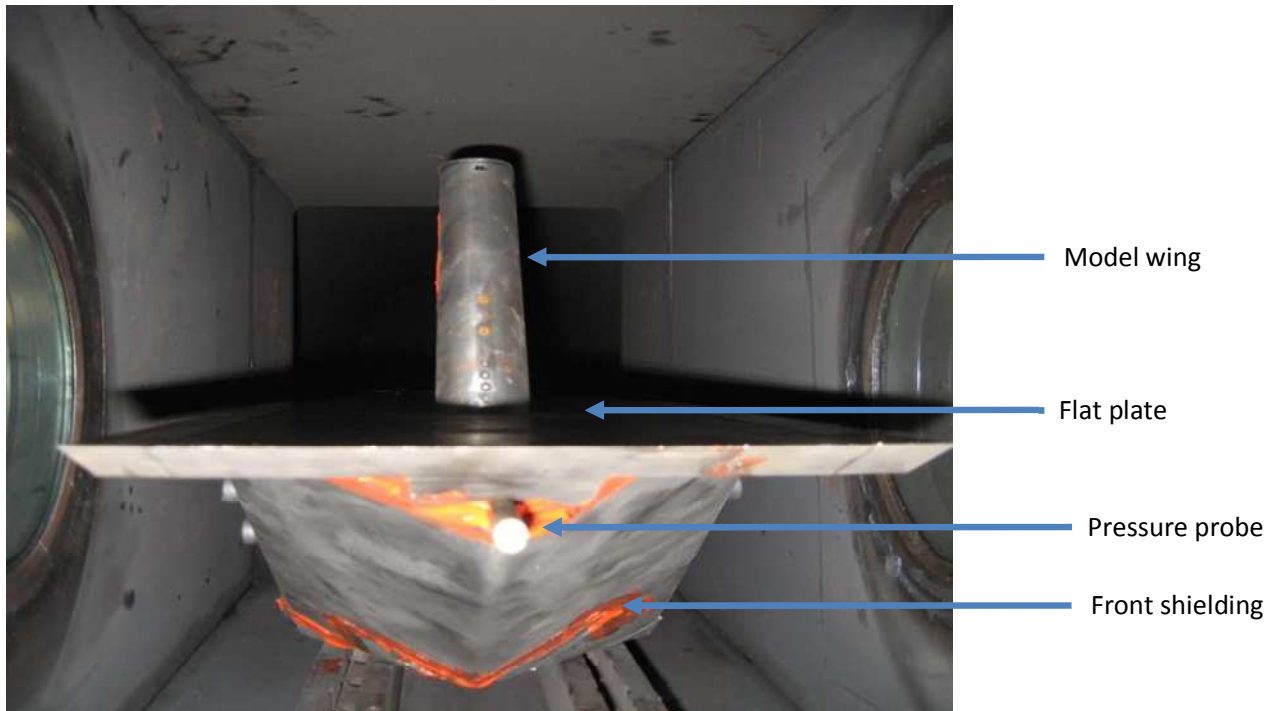


Figure 1-6: Final model configuration prior to the first shot, showing the wing, flat plate, stagnation pressure sensor and front wedge shielding. Note that this image has been vertically inverted for consistency with other representations of the model.

2. Heat flux gauge design and construction

2.1 Preliminary design considerations and theory

Thin film gauges were chosen to measure the heat flow due to both their ideal suitability (fast response) and the availability of suitable equipment at the Centre for Hypersonics for manufacturing these gauges.

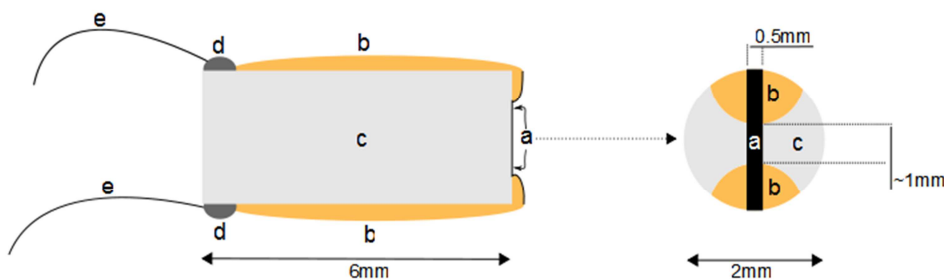


Figure 5: Conceptual Representation of a Thin Film Heat Flux gauge, showing the thin Nickel strip (a), gold conducting strips (b), Quartz substrate (c), soldered junction (d) and electrical leads (e).

The Auto 500 Sputtering system at UQ is an automated sputtering machine capable of producing extremely thin layers of metal and ceramic coating required to produce high quality thin film gauges. The gauges are typically composed of a ceramic substrate, on which a thin layer of metal is deposited via sputtering. Changes in electrical conductivity of the metal occur in response to changes in material temperature, and by modelling both the thickness of the film and the state and conductive properties of the ceramic substrate, it is possible to derive

extremely accurate and rapid heat flux measurements from the surface of the model. A conceptual representation of a thin film gauge is shown in Fig. 5.

The electrical resistance of the Nickel surface (at a in Fig. 5) is derived from the known material properties of Nickel. Since we now effectively have surface temperature as an input, we can derive the heat flux providing that we know the flow of heat leaving the surface and entering the substrate itself. As the flow of heat is closely approximated as being perpendicular to the gauge surface, a 1D approximation of the gauge will suffice:

$$\frac{\delta^2 T}{\delta x^2} = \frac{\rho C}{\kappa} \frac{\delta T}{\delta t}$$

Where ρ , C and κ represent the material density, heat capacity and conductivity respectively. While this partial differential equation cannot be solved directly, we can create a numerical analogue that will model the conditions at each time step. This relationship solved for heat flux at a given point in time, giving the following equation for heat flux:

$$\dot{q}(t) = \sqrt{\frac{\rho C K}{\pi}} \left[\sum_{i=1}^n \frac{T(t_i) - T(t_{i-1})}{\sqrt{(t_n - t_i)} + \sqrt{(t_n - t_{i-1})}} \right]$$

Equation 1: Fundamental equation use to derive heat flux from surface temperature readings of a gauge with known material properties.

An important fundamental distinction between the implementation of thin film gauges and other pressure and temperature probes is that the entire history of surface temperature measurements leading up to the current time, t , is required in order to obtain a reading of heat flux at t . This is in contrast to most pressure probes where a reading is only taken for the period where the flow has stabilised. However, although the accuracy of the equation is strongly dependant on the number of elements in the numerical analysis (represented by n), the wall time required to obtain an accurate heat flux reading from each gauge, that is to sum all the elements in the equation for every timestep and thin film gauge, is likely to be trivial, so it will be possible to convert the readings into heat flux rates immediately, allowing for only the heat flux and surface temperature readings at time steps of interest to be recorded.

2.2 Thin film Gauge construction

In practice, the construction of the thin film gauges is highly precise work, requiring meticulous accuracy in applying the metal film and the thin gold strips that conduct electrical signals from the connecting wires to the metal film on the gauge. While the application of the metal film (in this case Nickel) is greatly facilitated by the Auto 500 Sputtering System, the conducting gold film must be applied by hand using a thin brush and high purity gold paint.

The first step in constructing the gauges is to place 17-19 quartz rods of 2mm width into acrylic tubes with 1cm diameters. The quartz rods and acrylic tube are each roughly 30cm in length. The empty spaces between the rods and acrylic tube are filled with cyanoacrylate glue and allowed to set overnight. The tube is then cut into 6mm segments using a high precision rotary blade. These disks are then glued to flat acrylic plates in lots of 7 (accounting for roughly 120 quartz substrates), and polished on rotating beds with incrementally finer polishing

paper grit sizes of 240, 600 and finally 1200. After polishing and carefully inspecting the discontinuities in the quartz after each change in grit size, the disks are polished with a silk bed and 6 μ m diamond paste. The disks are then submerged in acetone for a period of 6 hours, allowing the cyanoacrylate glue to dissolve. The 6mm segments, which form the gauge substrate material, are then lightly etched in hydrofluoric acid to clean the surface of impurities and soften any remaining discontinuities in the quartz surface.

The substrates are then painted on both lateral sides with gold paste to form the conducting strips as per *b* in Figure 6. The painted substrates are then baked at 800°C to allow for the suspension agents in the gold paste to fully evaporate, leaving a thin gold layer on the substrates. Once painted with gold paste and baked to allow the particulates in the paint to evaporate, the substrates are placed in a mount, with the front end of each sensor facing 0.5mm wide slots. The mounted substrates are then placed in the Auto 500 Sputtering System and sputtered with Nickel, where electrical current is used to magnetically force ionised atoms of Nickel from a pure nickel target onto the quartz substrates (referred to as DC sputtering). The Auto 500 Sputtering System is set to sputter 1kÅ of nickel onto the substrate, which will yield an expected resistance of approximately 100 Ω across the film – the ideal value for the amplifiers used to convert the resistance into a digital signal. This yields a strip of width 0.5mm and length 2mm as defined by the width of the slots in the mount and the diameter of the substrates.

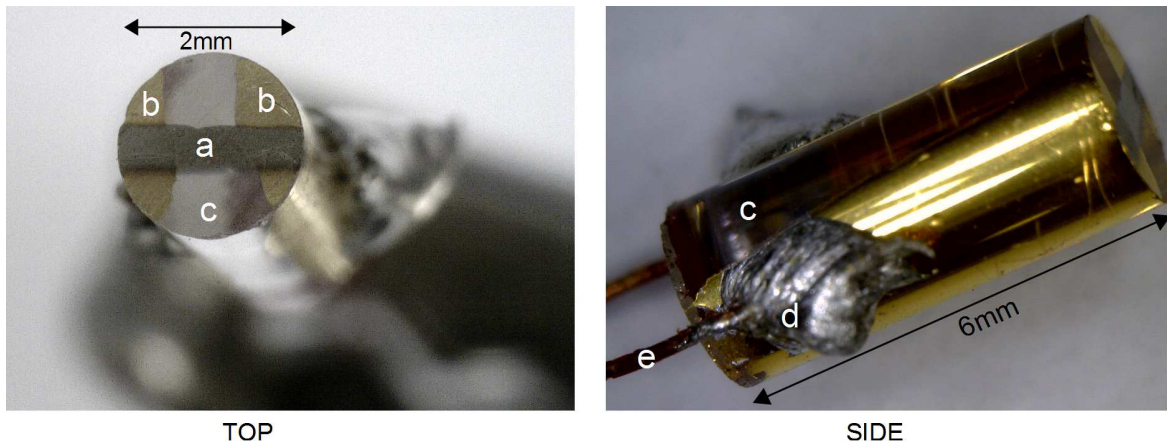


Figure 6: Microscopic photograph of the thin film gauges prior to calibration and mounting in the experimental model

Once the Nickel strip has been applied, a set of substrates is placed in a separate mount where their entire surface is exposed. Once in this configuration, the substrates are again placed in the Auto 500 Sputtering System and sputtered with a 5kÅ layer of SiO₂ (Silica) using RF sputtering – a method by which an electromagnetic field is used to force SiO₂ molecules from the target onto the substrates. While RF sputtering is significantly more time-consuming than the DC ionisation used to sputter Nickel, it is necessary when non-conducting materials are to be ionised. Silica is a strong electrical insulator that will shield the gauge from interference by ionised particles in the flow field, as well as affording the sensitive Nickel layer a degree of physical protection. Although the degree to which this insulating layer affects the fidelity of the gauge response is expected to be minimal, only a sample of the gauges will initially be sputtered with Silica to assess the exact delay and loss of precision in the thin film gauge response due to the Silica coating. If it is found that the life of the gauge and protection from

interference from ionised particles in the flow are not compromised by reducing the thickness of the Silica layer, then the amount of Silica applied to the gauges for final testing will be adjusted accordingly.

2.3 Thermocouple construction

Based on the expectation that the sub-micrometer thickness of the silicon dioxide layer used to protect the conductive element of the thin film gauges would not be sufficient to protect them during the test time if the surface were directly facing the flow (as would be the case for gauges on the wing), it was decided to replace the centerline of thin film gauges with thermocouples to ensure usable data. This decision was later vindicated by the rapid loss of the thin film gauges that were still kept on the wing during the tests.

In order to obtain heat flux values from the thermocouple voltage, the material properties of the electrode metals and of the mounting materials of the thermocouple itself must be known in order to convert the voltage into a surface temperature and then to obtain heat flux respectively.

Coaxial, E-type thermocouples were chosen for the experiment, due mainly to the relatively similar thermal properties of the materials used. This similarity in material properties reduces the error induced by the assumption of constant thermal properties in the semi-infinite reverse conductivity model used to deduce heat flux from surface temperature (see Equation 1). E-type thermocouples are composed chromel and constantan, for the negative and positive electrodes respectively. The sourced thermocouple materials were calibrated to confirm that the materials yielded the expected response of $63 \mu\text{V}/^\circ\text{C}$ (Schultz & Jones, 1973).

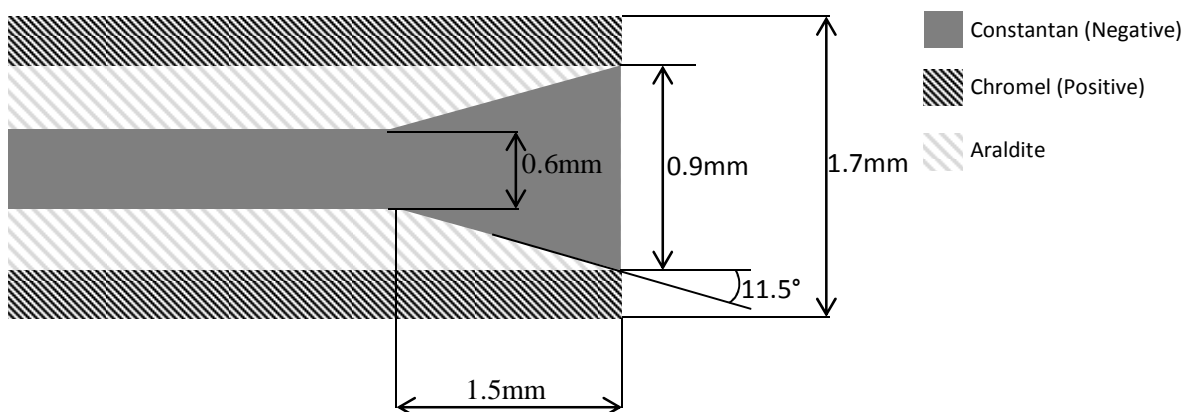


Figure 2-1: Material makeup of the thermocouple sensing tip and average dimensions provided by Brian Loughrey (the technician responsible for construction of the gauges).

Once the material properties of the electrodes were defined, it was possible to convert the thermocouple voltage response into a surface temperature reading, by means of multiplying the voltage reading by the sensitivity of the gauge. In order to convert the surface temperature into a heat flux reading, as per Equation 1, it is necessary to obtain density, heat capacity and conductivity values for the cross-sectional properties of the thermocouple. Due to tapering of the constantan electrode, the cross-sectional properties of the thermocouple are not constant in the axial direction (direction of heat flux). In order to simplify the modelling of the thermocouple, the cross-section expected to be most representative given the experimental conditions will be used. It will be assumed that incident heat by the end of the test time does not penetrate a significant distance

into the thermocouple, and that the thermal properties with respect to Equation 1 can be satisfactorily modeled by taking the mean cross-sectional properties at the surface of the thermocouple. The density, heat capacity and conductivities of constantan and chromel are illustrated below in Table 2-1.

Property	Value
<i>Constantan:</i>	
ρ (kg.m ⁻³) [8]	8920
C (J.kg ⁻¹ .K ⁻¹) [7]	401.0 (@273K)
κ (W.m ⁻¹ .K ⁻¹) [8]	21.171 (@373K)
<i>Chromel:</i>	
ρ (kg/m ³) [8]	8730
C (J.kg ⁻¹ .K ⁻¹) [7]	473.0 (@373K)
κ (W/m.K) [8]	19.2464 (@373K)

Table 2-1: Thermal properties of thermocouple materials Chromel, Constantan and Araldite, with values corresponding most closely to expected test conditions of ~300K.

In order to now obtain an effective thermal product, $\sqrt{\rho C \kappa}$, for the thermocouple materials, the thermal products for each of the constituent materials are averaged:

$$(\sqrt{\rho C \kappa})_e = \frac{(\sqrt{\rho C_p \kappa})_{\text{constantan}} + (\sqrt{\rho C_p \kappa})_{\text{chromel}}}{2} = 8808.47 \text{ J.m}^{-2}.\text{s}^{-1/2}.\text{K}^{-1}$$

Equation 2: Derivation of effective thermal product, $(\sqrt{\rho C \kappa})_e$, for the thermocouple materials.

The thermocouples were constructed by Brian Loughrey, a technician at the facility experienced in the manufacture of these gauges.

3. Analytical heat flux calculations

In order to characterize the maximum heat flux that the model will be exposed to, analytical solutions to the stagnation heat flux were calculated. Figure 3-1 shows a schematic of the wing root region of interest.

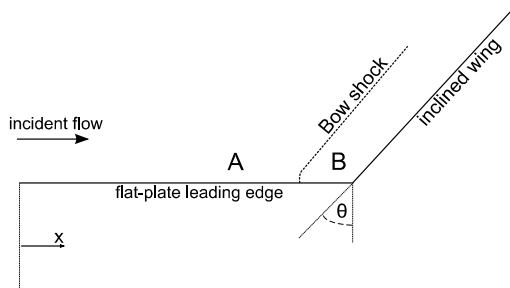


Figure 3-1: Schematic of the Wing Root experiment

Region A represents the Mach 8 free flow at 30km altitude. Based on the 1976 US Standard Atmosphere tables (National Oceanic and Atmospheric Administration, 1976), the atmospheric conditions at 30km altitude are as follows:

$$\begin{aligned}
\rho_A &= \rho_\infty = 0.018 \text{ kg/m}^3 \\
\mu_A &= \mu_\infty = 1.475 \times 10^{-7} \text{ kg/m.s} \\
a_A &= a_\infty = 301.7 \text{ m/s} \\
M_A &= M_\infty = 8 \\
u_A &= u_\infty = M_A \times a_A = 2413 \text{ m/s}
\end{aligned}$$

The heating in this area is characterised by a turbulent flat plate boundary layer, and will be low, relative to that in the interaction region or on the cylinder. The cylinder forming the wing can be modelled as a blunt body at an angle to the flow. We can therefore simplify the shock relations by taking the normal component of the incident Mach number, and using the resulting Mach number to predict conditions across the detached shock that will be formed by the cylinder (region B in Figure 3-1).

$$M_{n,A} = M_A \cos(\theta)$$

Where $M_{n,A}$ is the component of M_∞ normal to the cylinder, and θ is the wing sweep angle. Taking the oblique shock relations from Anderson Jr., 2006:

$$\begin{aligned}
\frac{\rho_B}{\rho_A} &= \frac{(\gamma + 1)M_{n,A}^2}{(\gamma - 1)M_{n,A}^2 + 2} = \\
\frac{p_B}{p_A} &= 1 + \frac{2\gamma}{\gamma + 1}(M_{n,A}^2 - 1) \\
M_{n,B}^2 &= \frac{M_{n,A}^2 + [2/(\gamma - 1)]}{[2\gamma/(\gamma - 1)]M_{n,A}^2 - 1}
\end{aligned}$$

where γ denotes the ratio of specific heats and is assumed to be 1.4 for air.

Taking the ideal gas relationship $\frac{T_B}{T_A} = \frac{p_B \rho_A}{p_A \rho_B}$ we can furthermore obtain the temperature rise immediately after the shock. Solving the above solutions for a Mach 8 flow through air yields the relative changes in pressure, temperature and density. By multiplying these relative values by the freestream conditions at Mach 8 and 30km altitude based on the US Standard Atmosphere data (as above), we can obtain the absolute values of temperature, pressure, density and Mach number directly behind the bow shock. These are shown for a range of sweep angles in Figure 3-2.

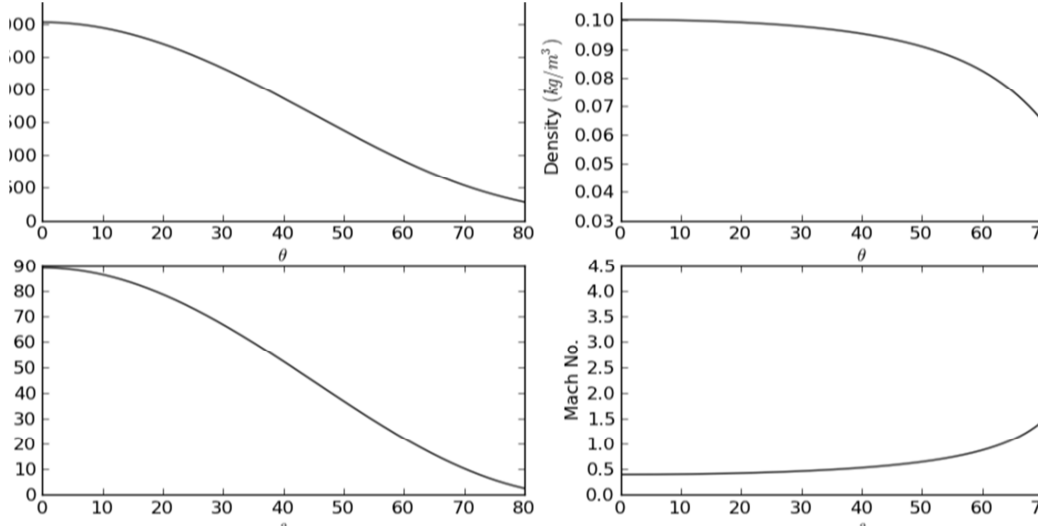


Figure 3-2: Analytical approximation of absolute conditions behind the bow shock of a swept wedge at varying sweep angles at a flow speed of Mach 8, with $\gamma=1.4$ and based on the 1976 US Standard atmosphere conditions for 30km altitude.

In order to produce an approximation for heat flux on the cylinder, we will use the analytical relations for stagnation point heating (Van Driest, 1956):

$$q_w = 0.57 Pr^{-0.6} (\rho_e \mu_e)^{1/2} \sqrt{\frac{du_e}{dx}} (h_{aw} - h_w)$$

Where the derivative of boundary layer edge velocity with respect to distance at the stagnation point, $\left(\frac{du_e}{dx}\right)_s$ can be closely approximated as (Anderson Jr., 2006)

$$\left(\frac{du_e}{dx}\right)_s = \frac{1}{R} \sqrt{\frac{2(p_e - p_\infty)}{\rho_e}}$$

The wall enthalpy is derived for a specific heat capacity of $1000 \text{ J.kg}^{-1}.\text{K}^{-1}$ for air with a wall temperature of 300 K (a valid assumption given the extremely short test times). The variation of stagnation point heating on the cylinder with increasing sweep angle based on standard atmospheric conditions at 30km altitude at Mach 8 is shown in Figure 3-3.

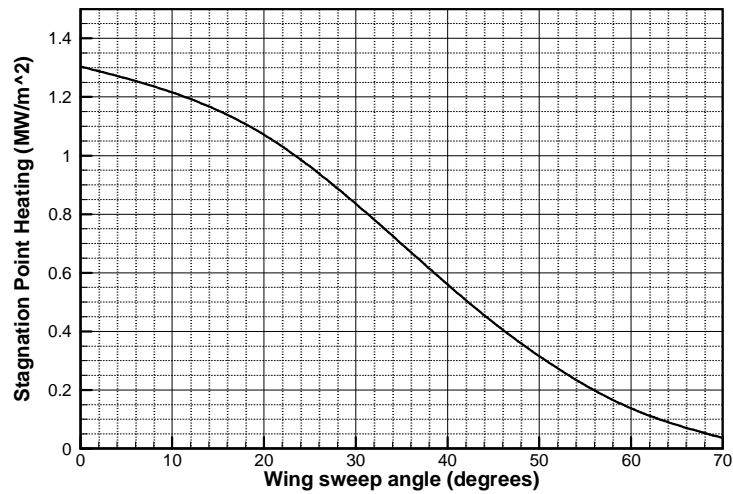


Figure 3-3: Stagnation point heat flux over the inclined cylinder for varying angles of sweep.

4. Experimental Campaign

4.1 Tunnel Conditions

The University's T4 test facility is a piston-driven shock tunnel. When a test shot is conducted, a free piston is driven by pressurized air from a reservoir, through a volume of gas in the compression tube, which ruptures a metal diaphragm of a fixed width causing the gas from the compression tube (the driver gas) to expand into the shock tube of the tunnel. The shock tube itself is filled with a defined pressure of air, which expands through a nozzle and over the model at some desired Mach number, temperature and pressure. In order to achieve the desired conditions, the reservoir pressure, compression tube pressure (and gas composition), shock tube pressure, nozzle type/shape and diaphragm width can be modified.

2 test conditions, called the "Low" and "High" pressure conditions were used in the campaign, with the pressures and gases used to operate the T4 test facility shown below in Table 4-1.

	Low Pressure condition	High Pressure condition
Test gas (shock tube)	100 % Air @ 130kPa	100 % Air @ 260kPa
Driver gas (compression tube)	100 % Argon @ 40.2ka	100 % Argon @ 80.5 kPa
Diaphragm	3mm mild steel	6mm mild steel
Reservoir	2.5 MPa	5.8 MPa

Table 4-1: High and low pressure fill conditions used.

The low pressure condition was chosen because the flow resulting from this condition was expected to represent the atmospheric conditions at 30km altitude most closely, given the available sets of conditions for which the tunnel has been certified to operate. The high pressure condition was chosen simply to represent conditions of comparatively higher heat flux, and would be used to assess whether or not the resulting measurements responded as expected.

The experimental campaign consisted of a total of 22 shots, representing the University of Queensland T4 Hypersonics facility shots 11043 to 11064. During the initial 10 shots of the campaign, a series of low pressure shots were conducted at sweep angles of 45° and 55°. The stability of the resulting voltage traces and schlieren photography indicated that the flow was not turbulent at these conditions. A small trip was constructed to ensure that the boundary layer would transition to turbulence, and the high pressure condition was introduced for the later shots, which included both high and low pressure conditions at 45°, 55° and 65° of sweep. The resulting conditions for each of the 22 shots are shown in Table 4-2.

Shot number	Reservoir (Mpa)	Driver gas (kPa)	Test gas (kPa)	Sweep	Trip
11043	2.5	40.2	130	45	no
11044	2.6	40.2	130	45	no
11045	2.6	40.2	130	45	no
11046	2.6	40.2	130	45	no
11047	2.6	40.2	130	45	no
11048	2.6	40.2	130	55	no
11049	2.6	40.2	130	55	no
11050	2.6	40.2	130	55	no
11051	2.6	40.2	130	55	no
11052	2.6	40.2	130	55	no
11053	5.6	80.5	264	55	no
11054	5.8	80.5	260	55	no
11055	2.6	40.2	130	65	no
11056	5.8	80.5	260	65	no
11057	2.6	40.2	130	65	yes
11058	5.8	80.5	260	65	yes
11059	5.8	80.5	260	65	yes
11060	2.6	40.2	130	65	yes
11061	5.8	80.5	260	55	yes
11062	2.6	40.2	130	55	yes
11063	2.6	40.2	130	45	yes
11064	5.8	80.5	260	45	yes

Table 4-2: Conditions for each of the 22 shots conducted. The blue shaded rows represent low pressure conditions, and the red shaded rows represent high pressure conditions. Shots 11043 and 11053 were the first of the condition, and slight changes were made in subsequent shots to ensure stable conditions during the test times.

While the exact resulting conditions cannot be measured directly for each shot, they were calculated using the measured pressure at the end of the shock tube, just prior to flow expansion over the model in combination with the known topology of the nozzle used to expand the flow. Calculations were performed using the

University's NENZFr (Nonequilibrium Nozzle Flow (reloaded)) code. The resulting conditions alongside the standard conditions, based on Mach 8 flow at 30km altitude, are shown below in Table 4-3. The values represent the mean of all shots excluding the first shot for the given condition (therefore excluding shots 11043 and 11053), with the tolerances indicating the absolute maximum deviation from the mean observed.

	Low Pressure Condition	High Pressure Condition	Standard Conditions
Temperature (K)	294.7 ± 27.8	376.9 ± 16.8	226.5
Pressure (kPa)	2.54 ± 0.10	4.89 ± 0.27	1.841
Density (kg/m ³)	0.026 ± 0.001	0.045 ± 0.002	0.0184
Total Enthalpy (MJ/kg)	3.31 ± 0.32	4.05 ± 0.16	2.91
Mach No.	7.37 ± 0.06	7.09 ± 0.18	8

Table 4-3: Test conditions for the low and high pressure condition, shown against atmospheric conditions at 30km altitude

4.2 Results

It was quickly discovered that the thin film gauges that were used in the wing did not survive the test time of the first shot. As the thermocouples did not experience major faults during the campaign it was still possible to obtain detailed heat flux data from the wing, albeit only in a linear configuration. As the conditions of interest include only shots where the flow was turbulent, only shots 11054 to 11064 will be shown here. Results will be broadly divided depending on the sweep angle used in the shot.

Note that due to the differences in magnitude of heat flux it was not possible to show all 2D flat plate measurements on the same scale, and each figure therefore has its own scale depending on the order of magnitude of the measured heat fluxes.

4.2.1 Results at 45° of sweep

Shots 11063 and 11064 were conducted at this angle, for the low and high pressure shots respectively. The resulting heat flux measurements of the thin film gauges and thermocouples on the flat plate and wing, respectively, are shown below in Figure 4-1 and Figure 4-2.

At this condition, the thermocouple at the base of the wing (recess 68 in Figure 1-3) was actually located underneath the flat plate, and therefore did not obtain usable data. This is unavoidable as the wing retracts into the body of the flat plate as sweep angle is decreased. By having a gauge beneath the flat plate at this condition it was possible to obtain measurements closer to the flat plate for higher sweep angles, where the wing is higher.

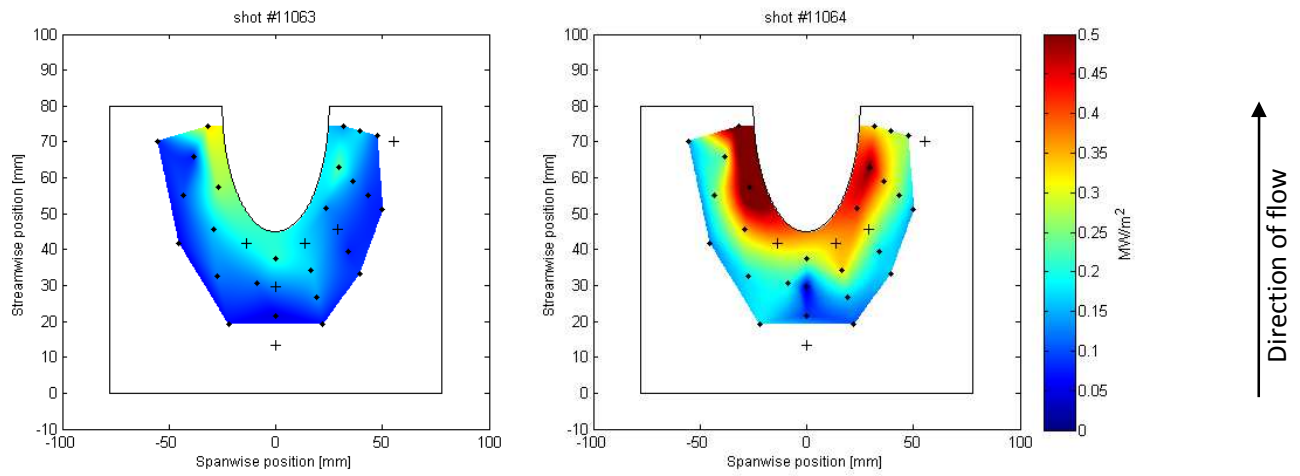


Figure 4-1: Heat flux map for the low (left) and high (right) pressure shots at 45° of sweep, shown on identical scales.

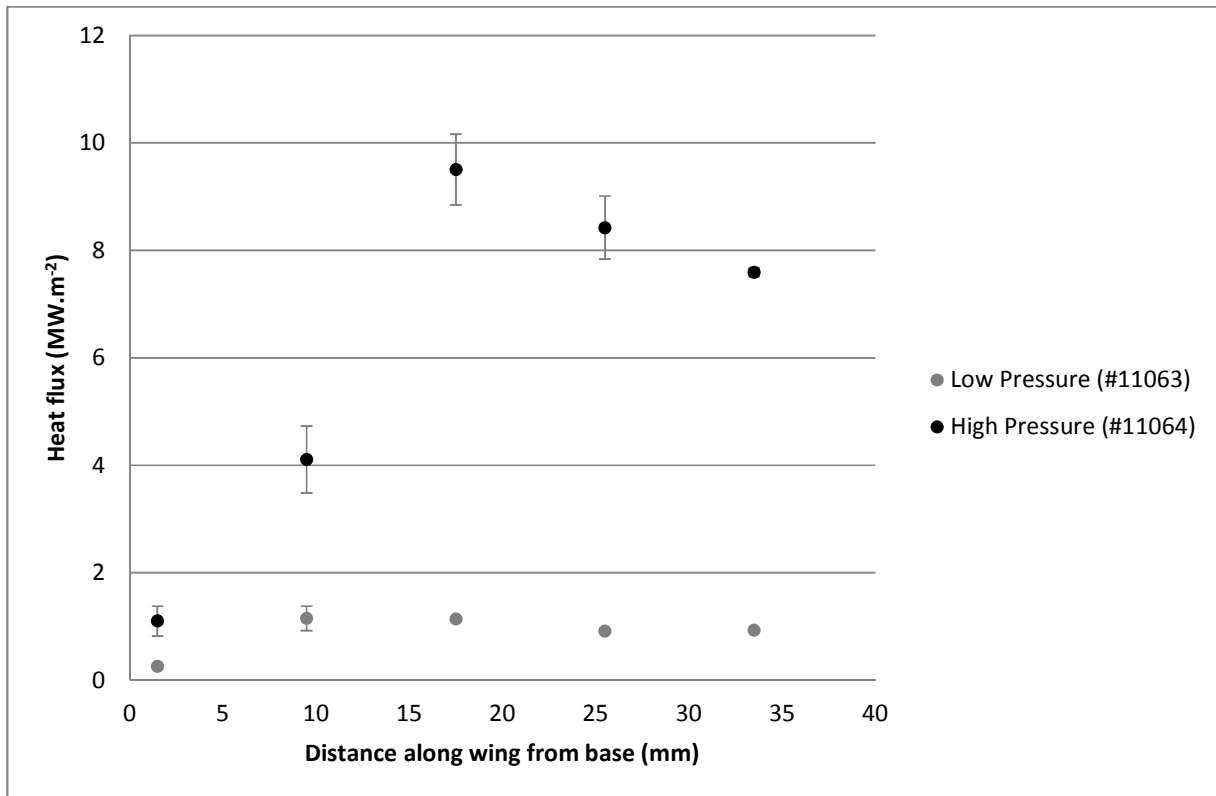


Figure 4-2: Heat flux measurements along the wing for high and low pressure shots at 45° of sweep, measured in distance from the flat plate region. Error bars represent the standard deviation over the test time.

Peak heat flux on the flat plate (observed at flat plate recess 2 from Figure 1-2) increased from $0.35 MW \cdot m^{-2}$ to $0.6 MW \cdot m^{-2}$, an increase of 70 %, when moving from the low to the high pressure condition. Heat flux on the wing (observed at the wing recess 71 from Figure 1-3 located at 18mm in Figure 4-2) increased by a greater

factor, peaking at $1.15 \text{ MW} \cdot \text{m}^{-2}$ for the low pressure condition and $9.5 \text{ MW} \cdot \text{m}^{-2}$ for the high pressure condition, an increase of 730%.

4.2.2 Results at 55° of sweep

This angle is represented by shots 11062 and 11061 for the high and low pressure shots respectively. The resulting heat flux measurements of the thin film gauges and thermocouples on the flat plate and wing, respectively, are shown below in Figure 4-3 and Figure 4-4.

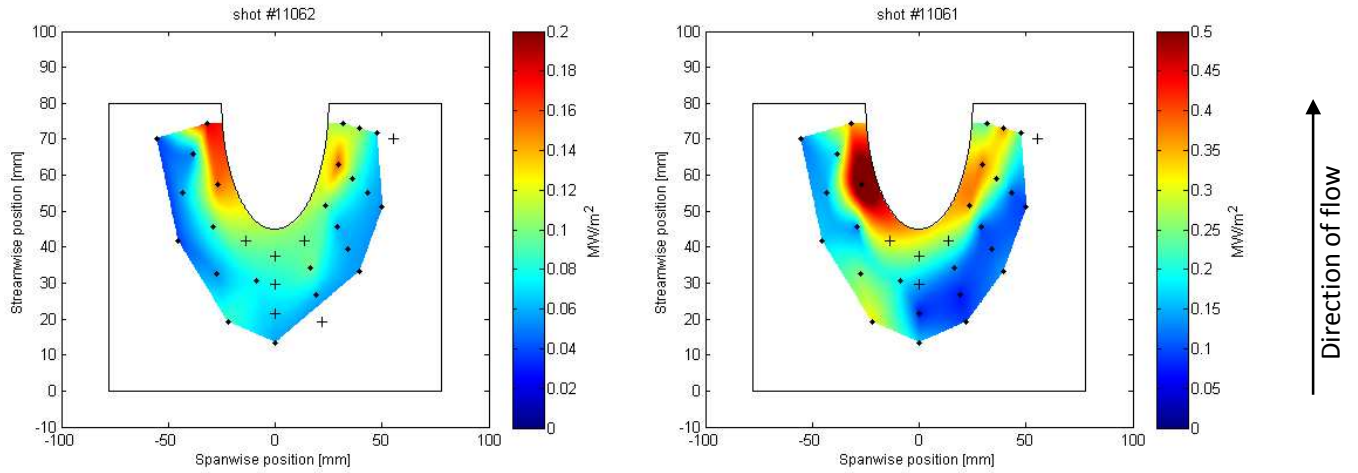


Figure 4-3: Heat flux map for the low (left) and high (right) pressure shots at 55° of sweep, shown on differing scales.

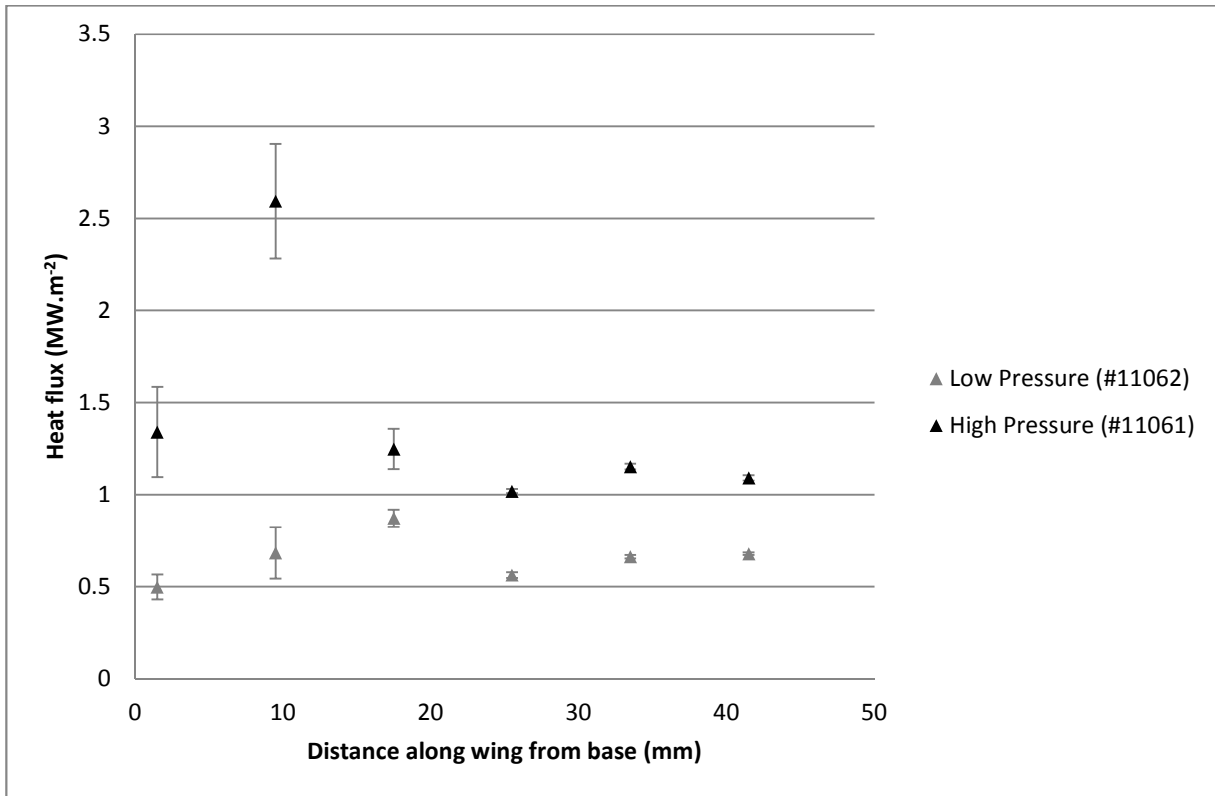


Figure 4-4: Heat flux measurements along the wing for high and low pressure shots at 55° of sweep, measured in distance from the flat plate region. Error bars represent the standard deviation over the test time.

Peak heat flux on the flat plate (observed at flat plate recess 5 from Figure 1-2) increased from $0.18 MW \cdot m^{-2}$ to $0.6 MW \cdot m^{-2}$, an increase of 230 %, when moving from the low to the high pressure condition. Heat flux on the wing (observed at the wing recess 69 and 70 from Figure 1-3, and located at 10mm and 18mm in Figure 4-2, for the high and low pressure conditions respectively) increased by a smaller factor, peaking at $0.87 MW \cdot m^{-2}$ for the low pressure condition and $2.59 MW \cdot m^{-2}$ for the high pressure condition, an increase of 200%.

4.2.3 Results at 65° of sweep

This was the highest sweep angle for which tests were conducted, and it is represented by shots 11058 and 11060 for the high and low pressure shots respectively. The resulting heat flux measurements of the thin film gauges and thermocouples on the flat plate and wing, respectively, are shown below in Figure 4-5 and Figure 4-6.

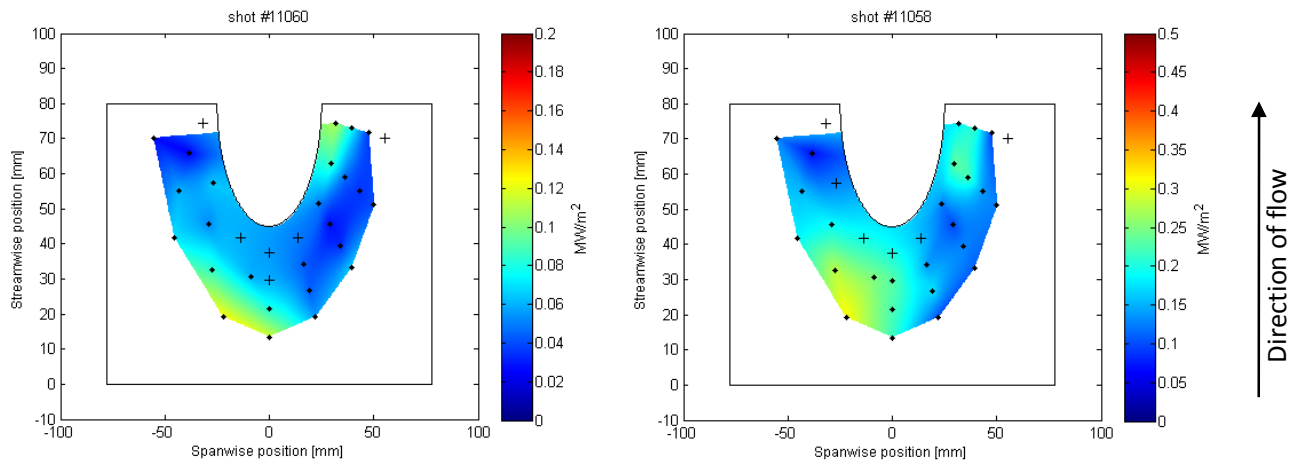


Figure 4-5: Heat flux map for the low (left) and high (right) pressure shots at 65° of sweep, shown on differing scales.

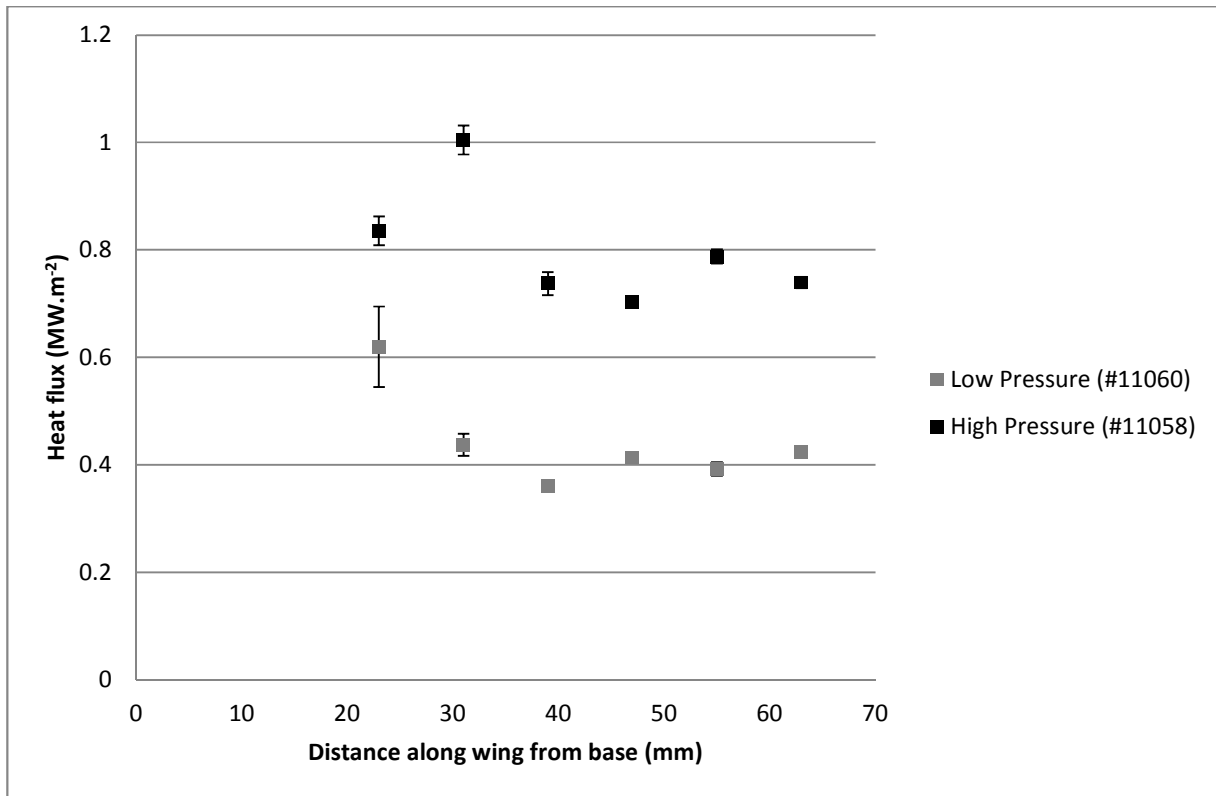


Figure 4-6: Heat flux measurements along the wing for high and low pressure shots at 65° of sweep, measured in distance from the flat plate region. Error bars represent the standard deviation over the test time.

For this configuration, a significant amount of heating was observed around recess 9. The magnitude of heating not near the base of the wing will be ignored in the definition of peak heating, but will be addressed in the discussion.

Peak heat flux on the flat plate (observed at flat plate recess 27 and 5 from Figure 1-2 for the low and high pressure conditions respectively) increased from $0.12 MW \cdot m^{-2}$ to $0.24 MW \cdot m^{-2}$, an increase of 100 %, when moving from the low to the high pressure condition. Heat flux on the wing (observed at the wing recess 68 and 69 from Figure 1-3, and located at 23mm and 31mm in Figure 4-2, for the high and low pressure conditions respectively) increased by an even smaller factor, peaking at $0.62 MW \cdot m^{-2}$ for the low pressure condition and $1.0 MW \cdot m^{-2}$ for the high pressure condition, an increase of only 60%.

5. Summary

In hypersonic flight the junction between wings or fins and the body of a vehicle can lead to localized regions of high heating. While the general topology of this flow has been established, confidence in the prediction of the heating rates is not high. The current study aims to improve the confidence of heat flux engineering relations by testing an experimental model of a wing/fin root in the T4 Shock Tunnel at the UQ Centre for Hypersonics. Thin film gauges and thermocouples were utilized to produce time-accurate, high resolution surface heat flux measurements.

While the results are still to be processed and compared to corresponding analytical and computational solutions for the actual conditions, some observations can already be made. Firstly, heat flux magnitude broadly increases with decreasing sweep. This is to be expected as the effective Mach number impinging perpendicularly on the wing increases with decreasing sweep, while the magnitude of the resulting stagnation at the base of the wing would also be expected to increase with lower sweep angles, thereby increasing the magnitude of heat flux on the flat plate as well. This appears to be the case for all both low and high pressure conditions, as is to be expected.

The high pressure conditions also tended to dramatically increase heat flux, as expected. An additional observation here is that in addition to affecting the magnitude of heat flux, variation in angle and condition also affected the location at which the peak heat flux occurred on the wing. This is of particular interest, because it is the peak heat flux which provides information about where shock impingement occurs. This in turn allows us to infer the size of the recirculation zone, if any, which is occurring at the root of the wing. Although the resolution of the wing heating data is quite limited (with the thermocouples separated by 18mm), it does appear that based on the 45° and 65° sweep angle scenarios the shock impingement, or peak heating, occurred farther from the wing root when moving from a low to high pressure condition.

The effect of the conditions on peak heating on the wing appeared to decrease with increasing sweep angle, with the relative peak heating for a high pressure shot at 700% for 45°, 200% for 55° and 60% for 65°. This interesting behavior makes sense intuitively, as one would expect the effect of the high pressure condition to asymptote to the effect of increased boundary layer heating alone as the sweep angle approaches 90°. There did not appear to be an observable pattern in the relationship between the effect of moving from low to high pressure conditions and the angle. However, a significant increase in overall heat flux could be observed when moving from low to high pressure, as well as for decreases in sweep angle, as is to be expected.

Finally, it should be noted that heating was observed on some of the outer thin film gauges (around recess 9 as per Figure 1-2). As this effect appeared to increase the heat flux of surrounding gauges as well, it cannot be

simply attributed to a faulty gauge at this location. It could be caused by a number of reasons, but the most logical appear to be:

1. Asymmetric turbulence effects coincidentally causing significant heating in this region.
2. Glue and sealant residue on the wing cause additional turbulence in the vicinity of those gauges

Further investigation and time-accurate visualization of the heat flux on the flat plate should be able to confirm that possibility 1 is not the cause for this phenomenon (it appears unlikely already given that the effect is in the vicinity of recess 9 in some of the other results as well). By observing time-accurate results, it will also be possible to infer if any anchoring or other similar effects suggest the presence of a disturbance near those gauges. This could be caused by excess sealant, which had to be applied generously at the corners and edges of the flat plate insert (and therefore close to the gauges themselves) to avoid any possible leakage of air into the body of the model, where it could potentially destroy the instrumentation.

Future work will focus on addressing some of the questions and issues raised in the represent report. Additionally, analytical and computational models will be built based on the actual conditions in the tunnel. Much of the significantly higher heat flux measured compared to expected values can be subjectively explained by the higher enthalpy, density, pressure and temperature experienced in the tunnel (see Table 4-3) as compared to actual atmospheric conditions. While this and other phenomena can be explained qualitatively given the available information, the next report will aim to quantify differences in observed and expected results, and draw conclusions about flow-field topologies resulting from the observations made during the test campaign.

Bibliography

- Anderson Jr., J. (2006). *Hypersonic and High-Temperature Gas Dynamics*. American Institute of Aeronautics and Astronautics.
- Cox, J. D., Wagman, D. D., & Medvedev, V. A. (1989). *CODATA Key Values for Thermodynamics*. New York: Hemisphere Publishing Corporation.
- Driest, V. E. (1956). The Problem of Aerodynamic Heating. *Aeronautical Engineering Review*, 26-41.
- Gaitonde, D., & Shang, J. (1997). Structure of a Supersonic Three-Dimensional Cylinder/Offset-Flare Turbulent Interaction. *Journal of Spacecraft and Rockets*, 294-302.
- Heiser, W. H., & Pratt, D. T. (1994). *Hypersonic Airbreathing Propulsion*. American Institute of Aeronautics and Astronautics.
- Higgins, A. (2008). *Comparison of Engineering Correlations for Predicting Heat Transfer in Zero-pressure-gradient Compressible Boundary Layers with CFD and Experimental Data*. Fishermans Bend: DSTO Defence Science and Technology Organisation.
- Incropera, F. P., DeWitt, D. P., Bergman, T. L., & Lavine, A. S. (2007). *Fundamentals of Heat and Mass Transfer, 6th Edition*. John Wiley & Sons.
- Morgan, R. G., Lourel, I., & Buttsworth, D. R. (2001). *Fast response coaxial type-E thermocouple gauges for the measurement of heat flux in expansion tubes*. Brisbane: University of Queensland, University of Southern Queensland.
- National Oceanic and Atmospheric Administration. (1976). *U.S. Standard Atmosphere, 1976*. Washington, D.C.: National Aeronautics and Space Administration, United States Air Force.
- Omega.com. (2005). *Physical Properties of Thermoelement Materials*. Retrieved September 01, 2012, from <http://www.omega.com/temperature/Z/pdf/z016.pdf>
- Schultz, D. L., & Jones, T. V. (1973). *Heat-transfer measurements in short-duration hypersonic facilities*. Oxford: NATO Advisory Group for Aerospace Research and Development.
- Wideman, J. K., Brown, J. L., Miles, J. B., & Ozcan, O. (1995). Skin-Friction Measurements in Three-Dimensional, Supersonic Shock-Wave/Boundary-Layer Interaction. *AIAA Journal Vol. 33, No. 5*, 805-811.